

Research Article

The Mid-Term Forecast Method of $F_{10.7}$ Based on Extreme Ultraviolet Images

L. Lei ^{1,2}, Q. Zhong ^{1,2}, J. Wang,² L. Shi,^{1,2} and S. Liu^{1,2}

¹National Space Science Center, Chinese Academy of Sciences, Beijing 100190, China

²University of Chinese Academy of Sciences, Beijing 100190, China

Correspondence should be addressed to Q. Zhong; zhongqz@nssc.ac.cn

Received 15 January 2019; Revised 22 March 2019; Accepted 16 April 2019; Published 13 May 2019

Academic Editor: Michael Kueppers

Copyright © 2019 L. Lei et al. This is an open access article distributed under the Creative Commons Attribution License, which permits unrestricted use, distribution, and reproduction in any medium, provided the original work is properly cited.

The solar radio flux at 10.7cm ($F_{10.7}$) is a direct monitor and an important indicator of solar variability, and $F_{10.7}$ is commonly used in empirical atmospheric models, ionosphere models, etc. The source regions of $F_{10.7}$ are mainly in the corona above the active regions, and the extreme ultraviolet (EUV) images reflect the coronal thermal structure. In this paper, an index is defined as P_{SR} based on the intensity values of solar EUV images to represent the coronal contribution to $F_{10.7}$. The Spearman correlation coefficient between the observed values of $F_{10.7}$ and P_{SR} is 0.85 in 304 Å EUV images. Based on the high correlation, an empirical model is constructed. Combining the EUV data of SDO/AIA and the twin STEREO/EUVI, solar full-disk EUV images can be generated, and the future 27-day values of P_{SR} can be calculated. Then, a realistic estimation of $F_{10.7}$ from 1 to 27 days in advance can be provided by the empirical model. Compared to the predictive values of $F_{10.7}$ by the 54th-order autoregressive models in 2012-2013, the error drop-rate of our model is 12.54%, and our method has significant advantages in the upcoming 3 to 27 days' forecast.

1. Introduction

$F_{10.7}$ is an index of solar radio flux at the frequency of 2800 MHz and the wavelength of 10.7 cm. There are primarily two kinds of radiation mechanisms: gyroresonance emission and bremsstrahlung emission [1–4]. Gyroresonance emission only occurs where the magnetic field is sufficiently strong. Schonfeld et al. [5] found that, on 2011 December 9, in the rising phase of Cycle 24, $8.1\% \pm 0.5\%$ of the variable component of the $F_{10.7}$ flux was associated with the gyroresonance emission mechanism, although this percentage varies significantly over the activity cycle. The strength of bremsstrahlung emission is related to the plasma density. Because the active regions and the flares are denser than the quiet Sun, the source regions of $F_{10.7}$ are mainly in the coronal heights above the active regions [6]. Livingston et al. [7] found that there is no more the linear relation traditionally assumed to exist between $F_{10.7}$ and the sunspot number during Cycle 24. Selhorst et al. [8] found that $F_{10.7}$ and the number of active regions correlate well during the period of 1992–2013. It may be caused that $F_{10.7}$ are more sensitive to weaker magnetic fields than those necessary to form sunspots, of the order of

1500 G. The observation of $F_{10.7}$ started in 1947, and it has never been interrupted. At present, the commonly used value of $F_{10.7}$ in the world is observed at local noontime (20:00 UT) by the Dominion Radio Astrophysical Observatory in Canada, and it is expressed in units of *sfu* (solar radiation flux density, $1 \text{ sfu} = 10^{-22} \cdot \text{W} \cdot \text{m}^{-2} \cdot \text{Hz}^{-1}$) [9].

The solar extreme ultraviolet (EUV) irradiance heats and ionizes the Earth's atmosphere. Because the EUV irradiance cannot be observed from the ground, $F_{10.7}$ has been used as a proxy to represent EUV [5]. The upper atmospheric models have the computer code which also use $F_{10.7}$ as the proxy for solar irradiances [10]. The model of upper atmosphere is commonly used to calculate the atmospheric density to the orbital prediction of low Earth orbit satellites, so it is necessary to input the future $F_{10.7}$ in the case of orbit prediction [11–13]. Therefore, the prediction of $F_{10.7}$ plays a major role in the accuracy of orbit prediction.

The approximately 11-year long-period and average 27-day mid-period variations have already been discovered in solar activity. The 11-year periodicity is the solar variational cycle, and the 27-day periodicity is due to the period of the

solar rotation [14]. Prediction of the solar radiation index should correspond with the periodic features of solar activity. Singular spectrum analysis (SSA) is a nonparametric spectral estimation method, which can be an aid in the decomposition of time series into a sum of components and forecast the time series by these components. SSA can be effectively used to analyze the time series with periodic oscillations [15]. In machine learning, an autoregressive model (AR-model) could learn from a series of timed steps and take the previous results as inputs for a regression model, in order to predict the value of the next time step [16]. Thus, Zhong et al. [17] and Liu et al. [18] used the SSA method and the 54th-order AR-model, respectively, to forecast 27-day $F_{10.7}$ because both the SSA method and the AR-model are suited to periodic and cyclical statistics. The methods of these two articles both showed predictive precision higher than that achieved by the United States Air Force (USAF) during the solar minimum in the Cycle 23. However, when a large active region (AR) rapidly appears on or disappears from the solar disk, the predictive precision of the 54th-order AR-model is unsatisfactory. Additionally, Wang et al. [19] proposed a mathematical method to extend the mid-term prediction of $F_{10.7}$ to as long as 54 days without the need for extra solar observation data.

$F_{10.7}$ is generated at coronal heights and related to the presence of active regions and the occurrence of flares [8]. Some empirical prediction models based on major solar features are described below. Wen et al. [20] forecast $F_{10.7}$ using the areas and positions of sunspots. Henney et al. [21] forecast $F_{10.7}$ utilizing advanced predictions of the global solar magnetic field generated by a flux transport model. The two prediction models above were constructed only using data from the Earth-side solar hemisphere; many scholars have focused on the far-side solar disk. Quémerais and Bertaux [22] forecast future 14-day $F_{10.7}$ using the interplanetary Lyman α background data obtained by the Solar Wind Anisotropies (SWAN) telescopes on board the Solar and Heliospheric Observatory (SOHO) [23]. Lindsey and Braun [24] used seismic maps of the far-side solar hemispheres for solar active regions (ARs) forecasting. Although the Lyman α background data and seismic maps of the far-side solar disk have the longer observed time span, the extreme ultraviolet (EUV) images of the twin Solar Terrestrial Relations Observatory (STEREO) spacecraft used in this study can show the far-side solar ARs more directly and describe their real-time variation characteristic more accurately.

The different wavelength EUV images are expected to observe the different regions of the solar atmosphere, such as the coronal hole (CH), quiet sun (QS), active region (AR), and flare plasma [25], and the values of $F_{10.7}$ have a high correlativity with the magnetic active regions [26]. $F_{10.7}$ can be visualized as viewing the chromosphere (electron temperature $\sim 10,000\text{K}$) through a lower corona of varying optical thickness due to the changing extent and density of the trapped coronal plasma overlying active regions and other active structures. For the discussion we formulate a new index, P_{SR} , which is a proxy for the low-coronal, free-free contribution to $F_{10.7}$, derived from the EUV data of the Atmospheric Imaging Assembly (AIA) on board

the Solar Dynamics Observatory (SDO) [27]. Balan et al. [28] demonstrated that the shorter (extreme ultraviolet and ultraviolet) and longer (10.7 cm) wavelength solar fluxes have a nonlinear relationship during entire solar cycles. This is because the decreasing presence of gyroresonant absorption compared with free-free emission at low activity levels and the contribution of the magnetic field strength below about 1500 Gauss to $F_{10.7}$ is undercounted [29]. Therefore, we define a function of $F_{10.7}$ in terms of P_{SR} . Furthermore, since February 2011, the entire far-side solar disk could be observed directly by the Extreme Ultraviolet Imager (EUVI) instruments, the telescopes in the two STEREO's Sun Earth Connection Coronal and Heliospheric Investigation (SECCHI) imaging suite [30]. The solar full-disk EUV images can be obtained by combining data from STEREO/EUVI with that of SDO/AIA. Then, the future 27-day values of P_{SR} can be calculated to forecast $F_{10.7}$. In this paper, an empirical method is constructed according to the ideas above to predict 27-day $F_{10.7}$ based on the EUV images.

The aim of this paper is to predict solar $F_{10.7}$ up to one Carrington rotation in advance utilizing full solar composite 304 Å EUV images from SDO/AIA and STEREO/EUVI. We first defined an index as P_{SR} based on the intensity values of solar EUV images to represent the low-coronal, free-free contribution to $F_{10.7}$. This paper importantly demonstrates the tangible benefits that 360 degree solar observations provide for the prediction of solar activity. This prediction method is found to perform better in the 3-27 days period, particularly in cases where active regions emerge on the far side of the Sun.

After introducing the background of forecasting $F_{10.7}$ in Section 1, Section 2 presents and analyzes the dataset and establishes the method. Section 3 contains the results and discussion, and Section 4 presents the conclusion.

2. Data Processing and Method Establishment

The two EUV channels (171 Å and 304 Å) of SDO/AIA are chosen, because they are also in STEREO/EUVI. The daily level-1 512×512 data FITS (Flexible Image Transport System) files of SDO/AIA from May 2010 to December 2015 are downloaded from the available database of the Joint Science Operations Center (JSOC) at Stanford University (<http://jsoc.stanford.edu/>), and the daily 512×512 data FITS files of STEREO/EUVI from January 2011 to December 2013 are downloaded from the available database of the website <https://stereoftp.nascom.nasa.gov/data/beacon/ahead/secchi/img/euvi/>.

The above data files are updated daily at approximately 20:00 UT, which corresponds to the observed time of the $F_{10.7}$ index. The FITS files are eliminated if their quality (FITS header keyword) is not equal to 0. The data files of $F_{10.7}$ can be downloaded from the websites of the National Oceanic and Atmospheric Administration (NOAA) (ftp://ftp.ngdc.noaa.gov/STP/space-weather/solar-data/solar-features/solar-radio/noontime-flux/penticton/penticton_observed/listings/listing_drao_noontime-flux-observed_daily.txt).

The SDO/AIA datasets from May 2010 to December 2015 are used to determine the form of the function between $F_{10.7}$ and P_{SR} . The SDO/AIA datasets of 2012-2013 and STEREO/EUVI datasets are taken as the testing sets.

2.1. Coronal Contribution to $F_{10.7}$. To match the EUVI data, the previous work should use the overlapping and interchangeable AIA and EUVI data to represent measurements from the same plasma [31]. This previous work has been developed as an automated procedure in the SSWIDL software routines (*ssc_form_euvi_synoptic.pro*). In this routine, to match the SECCHI/EUVI data, the SDO/AIA data has been processed by the following formulas:

$$\text{For } 171\text{\AA}, \text{data}_{out} = \text{data}_{aia} / \text{exptime} \times 1.1$$

$$\text{For } 304\text{\AA}, \text{data}_{out} = \text{data}_{aia} / \text{exptime} \times \text{ssc_get_aia_304_factor}(\text{date}_{obs})$$

The “ data_{aia} ” is the original SDO/AIA data; the “ exptime ” is the exposure time of SDO/AIA in seconds. The “ date_{obs} ” is date and time when observation of this image started. The parameter “1.1” is the rough conversion factor for AIA 171 Å images to EUVI 171 Å. The routine “*ssc_get_aia_304_factor.pro*” returns the rough conversion factor for AIA 304 Å images to EUVI 304 Å. Finally, the “ data_{out} ” is the SDO/AIA data which matches the SECCHI/EUVI data. To calibrate the datasets of three EUV cameras, all SDO/AIA datasets have been processed by the above routine and all our results of SDO/AIA are based on the “ data_{out} ”.

Vernazza et al. [32], Krista and Gallagher [33], and Pérez-Suárez et al. [34] found different solar regions (coronal holes, quiet sun, and active regions) corresponding to the different distributions in the intensity histogram of EUV images. Schonfeld et al. [5] showed that the EUV images collected by SDO/AIA could represent the bremsstrahlung component of $F_{10.7}$, so a proxy is defined in our paper to represent the coronal contribution to $F_{10.7}$ in EUV images by the following formula:

$$P_{SR} = \sum_{i=1}^n I_i, \quad \text{if } I_i \geq I_{SR}. \quad (1)$$

where I_{SR} is the pixel intensity threshold of source regions (SRs). The pixel point belongs to an SR if I_i is greater than or equal to I_{SR} . The parameter n is the sum of pixel numbers on the Earth-side EUV images, so P_{SR} is the integral effect of all SRs in the Earth-side corona.

The Spearman Regression correlation coefficient (R_S) is defined as the Pearson correlation coefficient between the ranked variables, and R_S assesses how well the relationship between two variables can be described using a monotonic function. R_S is computed from

$$R_S = \frac{\text{cov}(x, y)}{\sigma_x \cdot \sigma_y} \quad (2)$$

where $\text{cov}(x, y)$ is the covariance of the rank variables. σ_x and σ_y are the standard deviations of the rank variables [35, 36].

There is a nonlinear relationship between P_{SR} and $F_{10.7}$ [28], so the R_S between them in different I_{SR} values is to define the values of I_{SR} in the EUV images of two channels. The

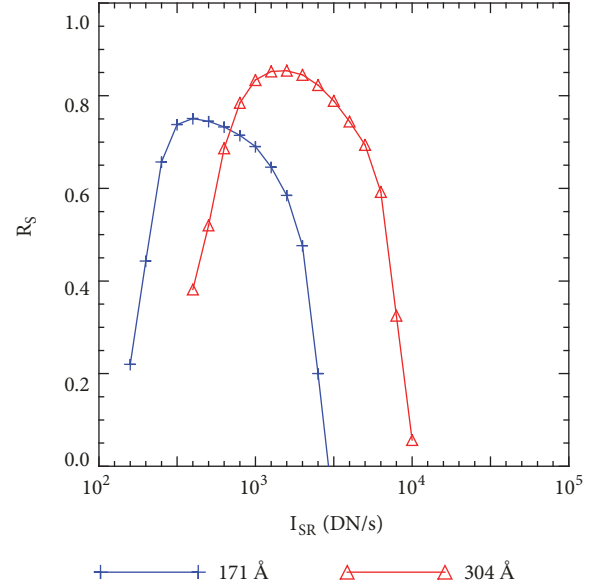


FIGURE 1: The Spearman correlation coefficients (R_S) between $F_{10.7}$ and P_{SR} , taking the specified pixel intensity as the threshold of the SRs in two channels' EUV images from May 2010 to December 2015.

results are shown in Figure 1. The max R_S values are 0.75 in 171 Å and 0.85 in 304 Å.

The 171 Å passband mainly reflects the upper transition regions and the quiet coronal regions of the solar atmosphere [27]. The 304 Å passband shows the upper chromosphere/transition regions and less variability with solar activity on a short time scale [37]. $F_{10.7}$ can be visualized as viewing the chromosphere (electron temperature $\sim 10,000\text{K}$) through a lower corona of varying optical thickness due to the changing extent and density of the trapped coronal plasma overlying active regions and other active structures [9]. The source regions of $F_{10.7}$ are closer to the regions of solar 304 Å than 171 Å, so the agreement between the $F_{10.7}$ and 304 Å is better than 171 Å. When I_{SR} is equal to $10^{3.2}$ DN/s in 304 Å, the R_S between P_{SR} and $F_{10.7}$ is up to 0.85. Thus, the pixels where intensities are greater than $10^{3.2}$ DN/s show some information about the $F_{10.7}$ source regions.

Based on the above analysis, the index associated with the $F_{10.7}$ source regions in 304 Å EUV images is defined as follows:

$$P_{SR,304} = \sum_{i=1}^n I_i, \quad \text{if } I_i \geq 10^{3.2} \text{ DN/S}. \quad (3)$$

The green part in Figure 2(b) shows where the $P_{SR,304}$ is on the EUV image. Most of this area covers the ARs, which is consistent with previous research: the source regions of $F_{10.7}$ are mainly in the corona above the active regions [5, 6].

2.2. Establishing the Method. Figure 3 shows the scatter diagram between $F_{10.7}$ and $P_{SR,304}$ from May 2010 to December 2015. Considering the exponential relationship between

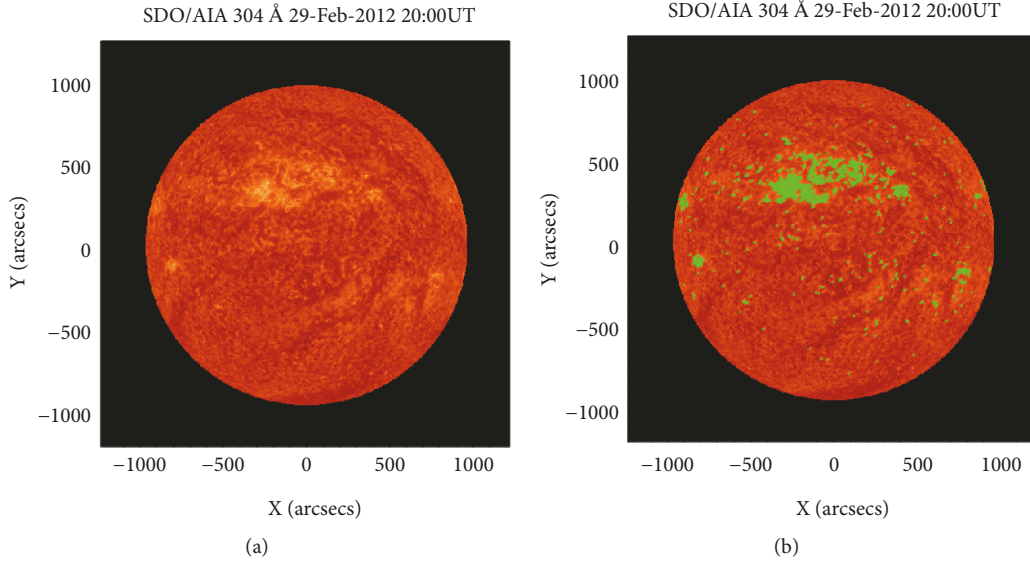


FIGURE 2: (a) The 304 Å EUV image on 29 February 2012; (b) pixels with intensities over $10^{3.2}$ DN/s (green dots).

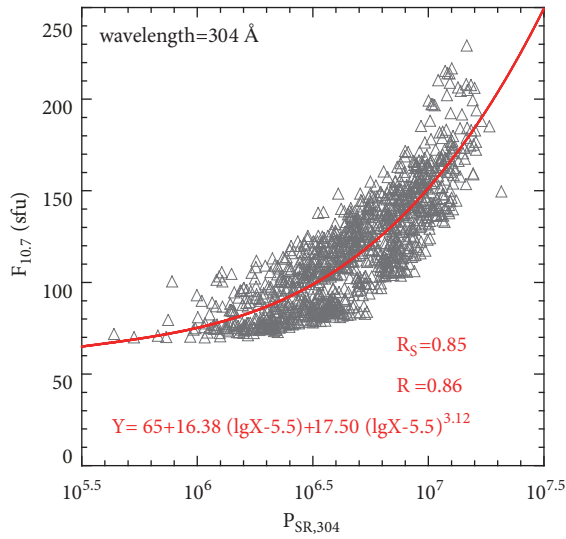


FIGURE 3: Scatter diagrams with the nonlinear function (solid red line) of $P_{SR,304}$ and $F_{10.7}$ from May 2010 to December 2015. The Spearman correlation coefficient (R_s) is between $P_{SR,304}$ and $F_{10.7}$, and the Pearson correlation coefficient (R) is between fitted Y and $F_{10.7}$. The function of the solid red line is $Y = 65 + 16.38(\lg X - 5.5) + 17.5(\lg X - 5.5)^{3.12}$.

$P_{SR,304}$ and $F_{10.7}$ in Figure 3, an empirical function of $P_{SR,304}$ and $F_{10.7}$ is defined as follows:

$$F_{10.7} = c + a_1 \cdot (\lg P_{SR,304} - 5.5) + a_2 \cdot (\lg P_{SR,304} - 5.5)^{a_3} \quad (4)$$

where c is a constant term that is expected to be the coronal base value. The parameters a_1 , a_2 , and a_3 are the undetermined coefficients.

To derive the best-fit coefficients for (4), all available daily $P_{SR,304}$ and $F_{10.7}$ from May 2012 to December 2015 are used for fitting by the nonlinear least square methods. The fitting function in Figure 3 is $Y = 65 + 16.38(\lg X - 5.5) + 17.5(\lg X - 5.5)^{3.12}$. The parameter “5.5” is the logarithmic total intensities while there is no active region on solar surface. That means the minimum value of $F_{10.7}$ is equal to 65 *sfu* while $\lg X$ equals 5.5. The higher order term means that the rate of $F_{10.7}$ increasing with $P_{SR,304}$ growth is nonlinear. To reduce the error of fitting function, we add a linear term. The correlation coefficient between fitted Y and $F_{10.7}$ is 0.86. In consideration of the degradation of EUV instruments, the parameters a_1 , a_2 , and a_3 are calculated by sliding fitting the daily $P_{SR,304}$ and $F_{10.7}$ of previous 14 CRs (Carrington rotations, ICR = 27 days) using the nonlinear least square methods. The correlation coefficient of sliding fitting is up to 0.92 (in Figures 10(a) and 10(d)); these are described in detail on the part three.

The STEREO/EUVI system provides a direct observation of the far side of the solar disk, showing areas which will rotate onto the side of the Sun visible from Earth in the next few days. There is a special IDL procedure for generating the full-disk EUV image (Figure 4) in the SolarSoft tree for STEREO (`$$$SW/stereo/ssc/idl/beacon/ssc_form_euvi_synoptic.pro`) that combines the 304 Å data from SDO/AIA with the data from STEREO/EUVI nearest to 20:00 UT. The “+” symbols under the numbers 0-27 in Figure 4 are the diurnal projection of the Earth on the solar surface along the Earth-Sun line from 27 March 2013 to 27 days later. The latitude and longitude of Earth’s projection can be calculated by the IDL procedure in the SolarSoft tree for STEREO (`$$$SW/stereo/gen/idl/spice/get_stereo_lonlat.pro`). The green regions show where the pixel intensities are greater than $10^{3.2}$ DN/s. The angle between the Earth-Sun line and the normal direction of pixel i in the EUV image is defined as $\alpha_{i,t}$. While the range of $\alpha_{i,t}$ belongs to $[0^\circ, 90^\circ]$, the pixel i is in the Earth-side disk. Then converting into the same coordinates

TABLE 1: The coefficients (a_t and b_t) and the correlation coefficient (R) of the fitting linear equation in Figure 5.

t (day)	$\lg(a_t)$	b_t	R	t (day)	$\lg(a_t)$	b_t	R
1	5.61	0.94	0.92	15	6.45	0.58	0.63
2	5.76	0.91	0.92	16	6.45	0.58	0.63
3	5.86	0.90	0.89	17	6.45	0.58	0.63
4	5.97	0.88	0.88	18	6.45	0.58	0.61
5	6.05	0.86	0.86	19	6.46	0.57	0.59
6	6.13	0.84	0.83	20	6.47	0.56	0.58
7	6.17	0.83	0.81	21	6.47	0.55	0.56
8	6.22	0.81	0.78	22	6.49	0.53	0.55
9	6.28	0.77	0.75	23	6.51	0.51	0.51
10	6.34	0.73	0.71	24	6.52	0.49	0.49
11	6.39	0.67	0.68	25	6.53	0.48	0.47
12	6.41	0.64	0.67	26	6.55	0.47	0.46
13	6.43	0.61	0.67	27	6.56	0.46	0.44
14	6.45	0.59	0.64				

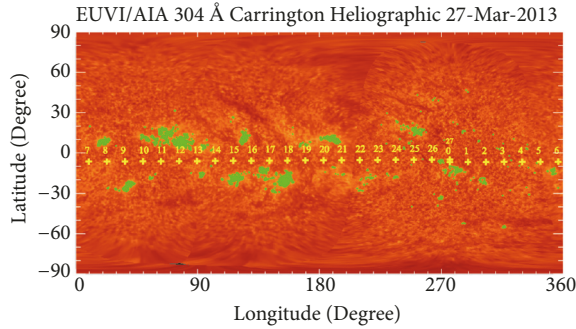


FIGURE 4: The 304 Å EUV image on 27 March 2013 from the combination of the 304 Å data from SDO/AIA with the data from the twin STEREO/EUVI. The coordinate is Carrington Heliography. The green regions represent the SRs of $F_{10.7}$, in which the pixel intensity is greater than or equal to $10^{3.2}$ DN/s. The gold plus signs represent the projected position of Earth at 27 March 2013 (in day 0) and within 1-27 days later.

with SDO/AIA images, the equivalent predictive $P_{SR,304}$ of the next 27 days from EUV images is defined as $W_{304,t}$ in (5).

$$W_{304,t} = \sum_{i=1}^n I_{i,t}, \quad (5)$$

if $I_{i,t} \geq 10^{3.2}$ DN/s, $t = 1, 2, 3, \dots, 27$

where the parameter t represents the day. The parameter $I_{i,t}$ is the intensity of pixel i in the next t days' image.

The area and intensity of AR will change in the next 27 days, especially in the solar maximum. The features of an AR's appearance, development, and disappearance are complex and unique. Therefore, the future values of $W_{304,i}$ are very difficult to forecast even though the far-side solar disk is observed before 13.5 days. So we compare the previous $P_{SR,304}$ with W_{304} on the same days to analyze the relationship between the $P_{SR,304}$ and W_{304} . For example, the value of $W_{304,1}$ on 27 March 2013 corresponds to the value of $P_{SR,304}$ on 28

March 2013. The first scatter diagram at the top left corner of Figure 5 shows the linear relationship between the values of $W_{304,1}$ from 2 January 2011 to 28 February 2013 and the values of $P_{SR,304}$ from 3 January 2011 to 1 March 2013. The last scatter diagram at the bottom right corner of Figure 5 shows the relationship between the values of $W_{304,27}$ from 2 January 2011 to 28 February 2013 and the values of $P_{SR,304}$ from 29 January 2011 to 27 March 2013. Even though the points disperse and the linear correlation coefficients dwindle with the growing parameter t , we assumed there are 27 kinds of linear relationships between the values of $W_{304,t}$ and $P_{SR,304}$ in the next 27 days, which is defined in (6). After adjusting for (6), the parameter $S_{304,t}$ is the corrected and predictive future 27-day values of $P_{SR,304}$.

$$S_{304,t} = a_t + b_t \cdot W_{304,t}, \quad t = 1, 2, 3, \dots, 27 \quad (6)$$

where a_t and b_t are the undetermined coefficients in the fitted linear equation (the green solid line in Figure 5), which are given in Table 1. The parameter t represents the day. Finally, the values of $F_{10.7}$ can be predictive 27 days in advance through substitution of $S_{304,t}$ for $P_{SR,304}$ in (4).

3. Results and Discussion

In the application, there is no data after the forecasting date. Only the daily $P_{SR,304}$ and $F_{10.7}$ before the forecasting date can be used to obtain the best-fit coefficients for (4). The correlation between Y and $F_{10.7}$ is performed for a certain number of Carrington rotations (CRs) before the start date of the series. This date is then advanced one day at a time through 2012 and 2013, generating a new correlation on each day. The minimum, average, and maximum correlation from this series is then recovered for that fitting window. The fitting window is varied from 1 to 28 CRs to generate Figure 6. The minimal correlation coefficient (R_{\min}) reaches the maximum in 14 CRs, and the three parameters R_{\max} , R_{mean} , and R_{\min} are steady after 14 CRs. Thus, the length of the fitting window is 14 CRs.

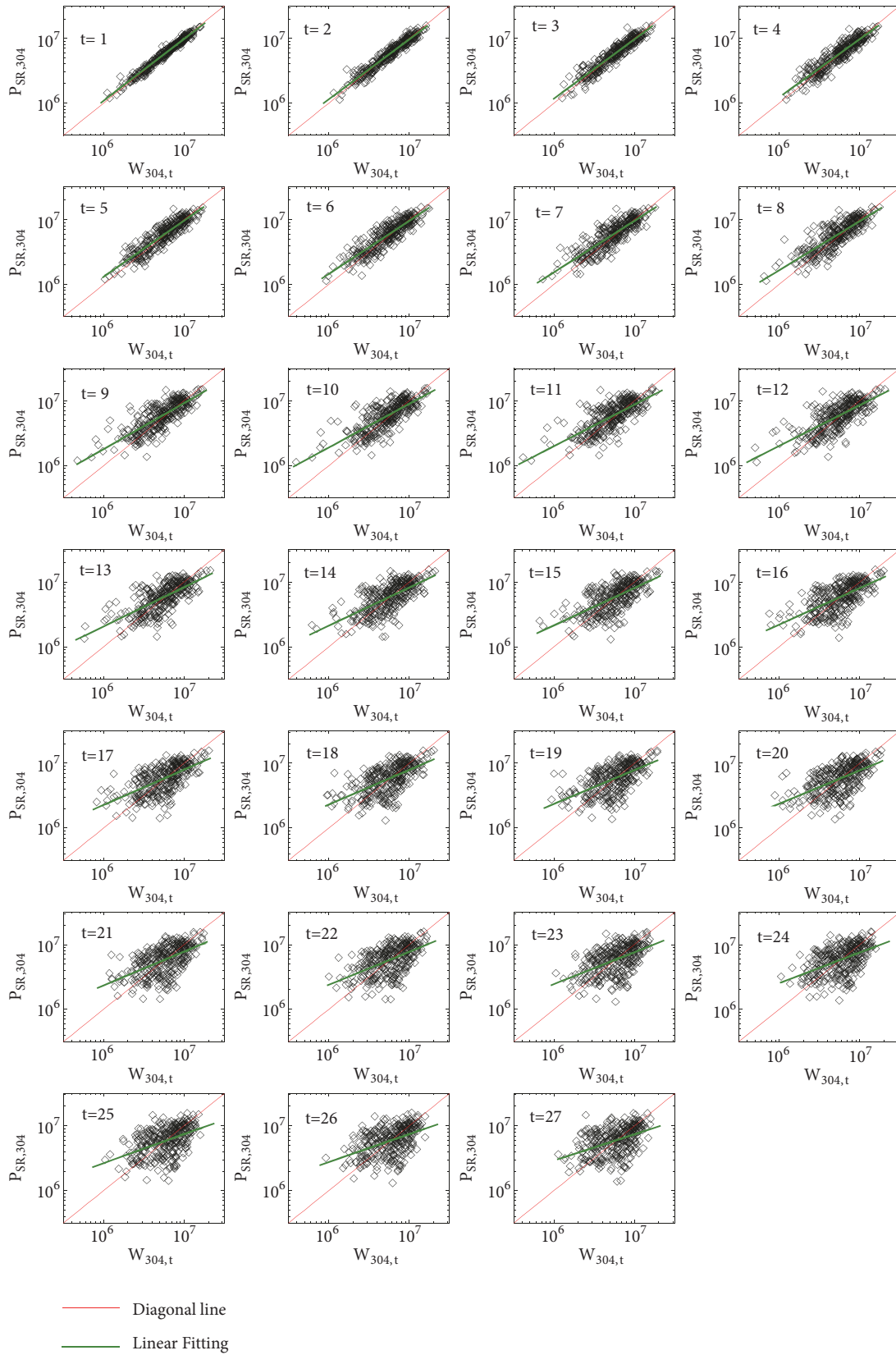


FIGURE 5: Scatter diagrams between $W_{304,t}$ and $P_{SR,304}$ before 27 March 2013. The solid red line is the diagonal line, and the solid green line is the fitting line.

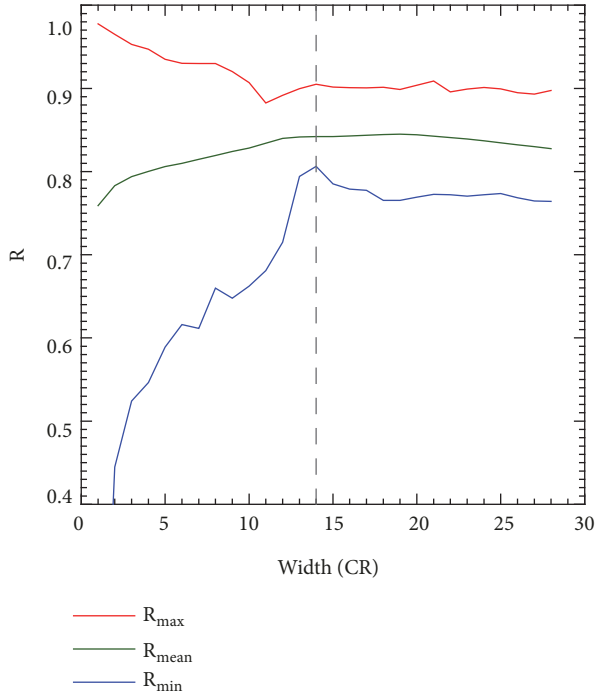


FIGURE 6: The correlation coefficient between fitted Y and $F_{10.7}$ with different widths in moving fit from 2012 to 2013. R_{\min} (blue line), R_{\max} (red line), and R_{mean} (green line) correspond to the minimum, maximum, and average of the correlation coefficient, respectively.

The 0-day predictive and observed $F_{10.7}$ values are compared in Figure 7. The 0-day predictive values are consistent with the observed $F_{10.7}$ values, especially from August 2012 to August 2013. The mean relative daily forecast error is defined as E_{mr}^t in (7). The 0-day forecast relative errors (E_{mr}^0) of our method are 5.49% in 2012, 4.86% in 2013, and 5.18% in 2012-2013.

$$E_{\text{mr}}^t = \frac{1}{N} \sum_{i=1}^N \frac{|o_{t,i} - f_{t,i}|}{o_{t,i}} \times 100\%, \quad t = 0, 1, 2, 3, \dots, 27 \quad (7)$$

where the parameter N , which represents the number of testing samples, is equal to 611 in 2012-2013. The parameter t represents the day, and $o_{t,i}$ and $f_{t,i}$ denote the observed and predictive values, respectively.

To show the precise of our prediction, Figure 8 shows a comparison of the 54th-order AR-model and our method with respect to the average daily predictive relative errors in advance of 1-27 days. The predictive $F_{10.7}$ values of 54th-order AR-model are calculated with the method of Liu et al. [18].

The two kinds of E_{mr}^t increase with the growth of advance time. While the error of our model increases with a steady rate in 1-27 days, the other error grows faster in 1-9 days and approximates to horizontal lines in 10-27 days. From the contrast, it is discovered that there are two kinds of fitting errors in our model: one is in (4), and the other is in (6). E_{mr}^0 in our method is the error of fitting in (4), which is up to 5.18%, and the E_{mr}^1 of AR-model is below 4%. Thus, the $F_{10.7}$ short-term predictive precision of our model is lower than that of AR-model. The reason is that the known preceding

value has the tallest weight in the predicted value of AR-model, and the $F_{10.7}$ varies slowly and autocorrelates very strongly. Therefore, the E_{mr}^t in our method is greater than that in the AR-model for 1-3 days. The growth rate of E_{mr}^t in our method is the error of fitting in (6). Even so, because of the addition of solar back disk data in our model, the accuracy of prediction is improved obviously for 4-27 days.

There are two classical evaluation indicators used to reflect the errors of the predictive results: the mean absolute error and the mean relative error. To assess the accuracy of every testing case, the errors are defined as follows:

$$E_{\text{mr}} = \frac{1}{27} \sum_{t=1}^{27} \frac{|o_t - f_t|}{o_t} \times 100\%, \quad t = 1, 2, 3, \dots, 27 \quad (8)$$

$$E_{\text{ma}} = \frac{1}{27} \sum_{t=1}^{27} |o_t - f_t|, \quad t = 1, 2, 3, \dots, 27 \quad (9)$$

where o_t and f_t denote the observed and predictive values, respectively, and the parameter t is the day.

To assess the accuracy of all testing cases, another two kinds of error are defined in (10) and (11).

$$ME_{\text{mr}} = \frac{1}{27N} \sum_{t=1}^{27} \sum_{i=1}^N \frac{|o_{t,i} - f_{t,i}|}{o_{t,i}} \times 100\%, \quad (10)$$

$$t = 1, 2, 3, \dots, 27$$

$$ME_{\text{ma}} = \frac{1}{27N} \sum_{t=1}^{27} \sum_{i=1}^N |o_{t,i} - f_{t,i}|, \quad t = 1, 2, 3, \dots, 27 \quad (11)$$

where the parameter N represents the number of testing samples, t represents the day, and $o_{t,i}$ and $f_{t,i}$ denote the observed and predictive values, respectively.

To assess the drop-rate between our model and AR-model, the parameters DR_{mr} and DR_{ma} are defined as follows:

$$DR_{\text{mr}} = \frac{ME'_{\text{mr}} - ME''_{\text{mr}}}{ME'_{\text{mr}}} \times 100\% \quad (12)$$

$$DR_{\text{ma}} = \frac{ME'_{\text{ma}} - ME''_{\text{ma}}}{ME'_{\text{ma}}} \times 100\% \quad (13)$$

where the ME'_{mr} and ME'_{ma} represent ME_{mr} and ME_{ma} of AR-model, respectively, during 2012-2013. ME''_{mr} and ME''_{ma} represent the ME_{mr} and ME_{ma} of our model, respectively, during 2012-2013.

Figure 9 shows the observed values of $F_{10.7}$ and the values of E_{mr} in the 54th-order AR-model and our method during 2012-2013. Due to the uncontrolled spin of satellites, instrument failure, or their inappropriate relative positions, SDO and the twin STEREO spacecraft cannot capture the full-disk EUV images clearly and completely, which should be omitted from the testing sample set (yellow vertical short line at the top in Figure 9). Finally, there are 611 samples for testing during 2012-2013, with 304 samples in 2012 and 307 samples in 2013.

The tendencies of E_{mr} in the two methods are approximated in Figure 9. The E_{mr} of our method is slightly less than

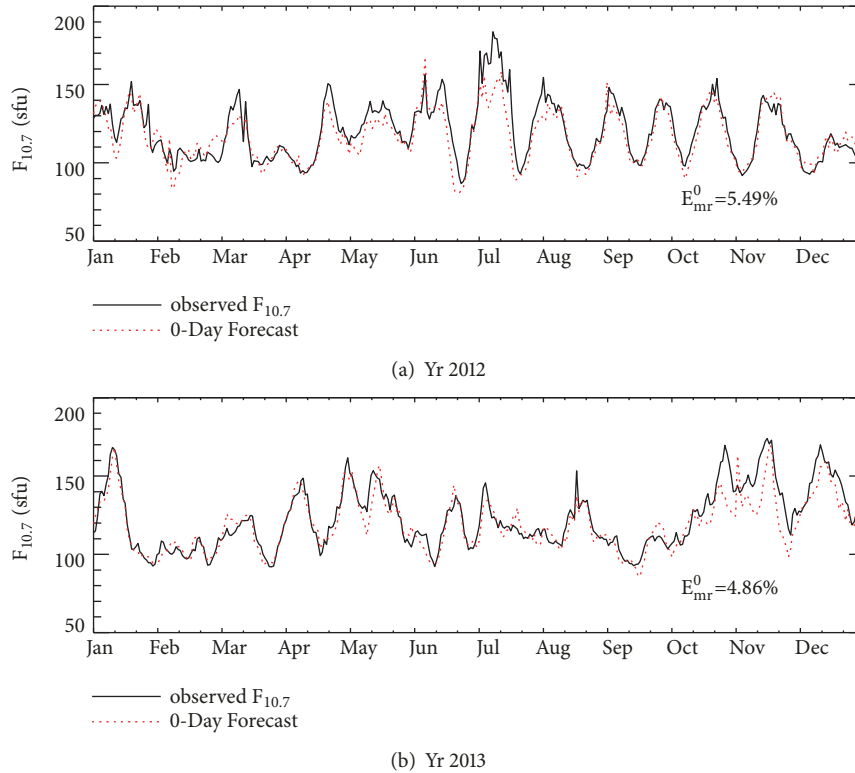


FIGURE 7: A comparison of 0-day predictive (dotted red line) and observed (solid black line) $F_{10.7}$ in 2012 (a) and 2013 (b).

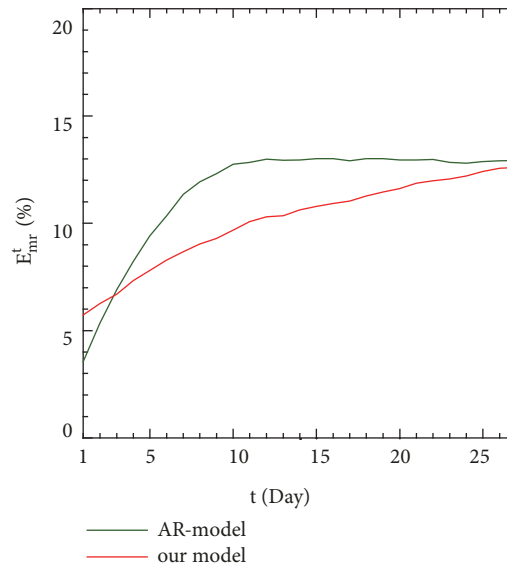


FIGURE 8: The E_{mr}^t of AR-model (green line) and our method (red line) during 2012-2013 for 1-27 days.

that of AR-model, especially during June 2012 and October 2013. A threshold of 10% E_{mr} is defined here to evaluate the accuracy of the forecasting results.

The E_{mr} in our method is less than 10% from July to November in 2012, which means that the prediction of our method is satisfied when the period of $F_{10.7}$ is stable. Compared with the ME_{mr} in the 54th-order AR-model, that

in our method decreases from 11.54% to 10.09% with a 12.52% drop-rate during 2012-2013 (shown in Table 2). The drop-rate of ME_{ma} is up to 10.35%. Table 2 shows that the accuracy of our method is desirable during testing. Additionally, two forecasting cases are chosen for further analysis in Figure 10.

The E_{mr} in our method is much less than that of the 54th-order AR-model in the case of 25 March 2013. Figure 10(a)

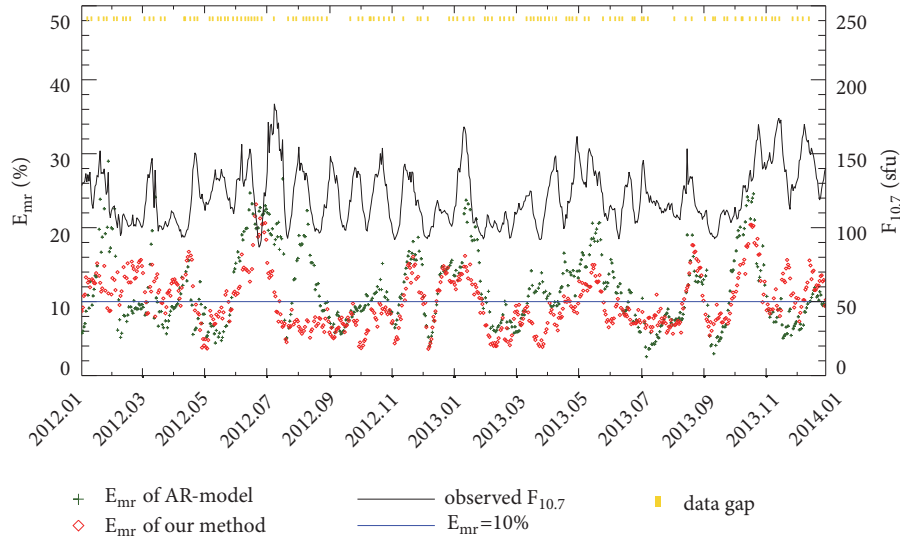


FIGURE 9: E_{mr} derived by the 54th-order AR-model (green plus signs) and our method (red diamonds) during 2012-2013. The solid black line represents observed $F_{10.7}$, and the solid blue line represents E_{mr} equal to 10%. The short yellow vertical line at the top represents missing data due to the incomplete EUV images.

TABLE 2: The ME_{ma} and ME_{mr} values of AR-model and our method during 2012-2013.

		Year			Drop-rate ^a (%)
		2012	2013	2012-2013	
ME_{mr} (%)	AR-model	11.91	11.17	11.54	
	Our method	10.28	9.91	10.09	12.52
ME_{ma} (sfu)	AR-model	14.25	14.09	14.17	
	Our method	12.67	12.74	12.71	10.35

^a The drop-rate is defined in (12) and (13).

shows a scatter diagram of observed $P_{SR,304}$ and $F_{10.7}$ in the previous 14 CRs and the future 27 days. The fitting line in Figure 10(a) is fitted by the data of the previous 14 CRs. The correlation coefficient (R) between fitted Y and $F_{10.7}$ is as high as 0.92. Figure 10(b) shows a comparison of observed $F_{10.7}$, $P_{SR,304}$, $W_{304,t}$ and $S_{304,t}$ in the previous and future 27 days from the test date, 25 March 2013. Figure 10(c) shows a comparison of observed and predictive $F_{10.7}$. The results of our method are closer to the observed $F_{10.7}$ than that of the 54th-order AR-model. The ARs (NOAA 11711, 11715, 11716, 11717, and 11718) on the Earth-side SDO/AIA EUV images on 8 April 2013 (Figure 11(c)) were already captured 14 days in advance by the EUV images on 25 March 2013 (Figure 11(a)). Additionally, these ARs move towards the Earth without disappearance, and no new ARs appear. In summary, when the ARs on the far-side EUV images change slowly in the next Carrington rotation, the forecast accuracy of our method is preferable to that of AR-model. This is the greatest advantage of our model in comparison to the AR-model.

Another case on 28 February 2012 is shown in Figures 10(d), 10(e), and 10(f). There is a crest of $F_{10.7}$ from 1 to 14 March 2012 along with a trough of $W_{304,t}$ and $S_{304,t}$ (see

Figure 10(e)). Contrasting the three images in Figure 12, new ARs (NOAA 11429 and 11430) appear, but they are too weak in the solar full-disk EUV image (Figure 12(a)). These ARs then strengthen while they rotate towards the Earth on 8 March 2012 (Figure 12(c)). E_{mr} of our method decreases from 15.65% on 28 February 2012 to 8.45% on 6 March 2012, as seen in Figure 13. Our model could recognize the approximate position of NOAA 11429 and 11430 on 4 March 2012 because the forecast values of $F_{10.7}$ remain close to the observed values after 14 March 2012 (corresponding to 10, 9, and 8 on horizontal axis in Figures 13(d), 13(e), and 13(f), respectively). Thus, once the solar full-disk EUV image captures the new SRs, the forecast results of our model are adjusted rapidly, and the predictive precision is improved quickly. This is the second advantage of our model in comparison to the AR-model.

In comparison with AR-model in Figures 10(c) and 10(f), the accuracy of prediction is unsatisfactory in the coming 1-2 days. This finding agrees with the results in Figure 8. Thus, to gain a more satisfactory predictive precision, we can combine the upcoming 1-2 days predictive values of the 54th-order AR-model with the upcoming 3-27 days predictive values of our method in practice.

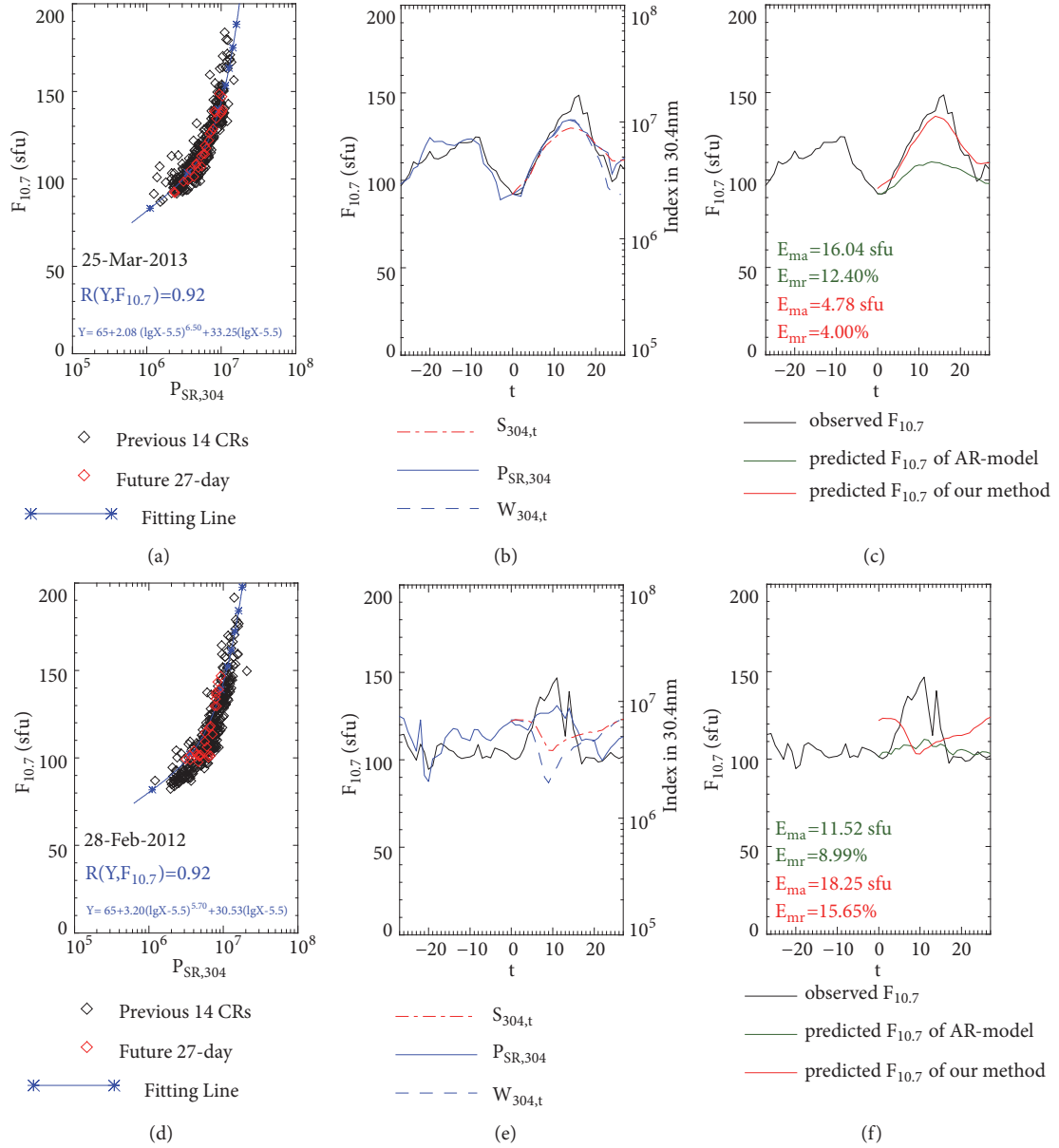


FIGURE 10: The $F_{10.7}$ forecast results of two cases: 25 March 2013 (a, b, c) and 28 February 2012 (d, e, f). (a, d) Scatter diagrams of the 14 CRs' previous values of $F_{10.7}$ and $P_{SR,304}$ (black diamonds), and the future 27-day values of $F_{10.7}$ and $P_{SR,304}$ (red diamonds). The solid blue line with asterisks is the fitted function. R is the correlation coefficient between fitted Y and $F_{10.7}$. (b, e) Comparison of $P_{SR,304}$ (solid blue line), W_{304} (dashed blue line), S_{304} (dashed-dot red line), and $F_{10.7}$ (solid black line) in previous (negative value in horizontal axis) and future (positive value in horizontal axis) 27 days of that test date (zero in horizontal axis). (c, f) The value of observed $F_{10.7}$ (black line) and predictive $F_{10.7}$ obtained from the 54th-order AR-model (green line) and our method (red line) in future (positive value in the horizontal axis) 27 days.

4. Conclusion

Through the error analysis and case studies on the medium-term forecast experiments of daily $F_{10.7}$ during 2012-2013, we can obtain the following conclusions.

The full-disk EUV images can provide coronal information about the far-side solar disk, which is 13.5 days earlier than that of other models using only Earth-side information or $F_{10.7}$ itself. Thus, the $F_{10.7}$ medium-term forecast accuracy

of our method is better than that of the 54th-order AR-model, especially for upcoming 3-27 days.

The sensitivity of our model is much higher than that of AR-model. The forecast results of our model can adjust rapidly, and the predictive precision is improved quickly. The drop-rate of ME_{mr} in our method is 12.52% during 2012-2013.

This was the first attempt in which we found a proxy in solar EUV images to represent the coronal contribution to $F_{10.7}$. It was also the first attempt to forecast the upcoming

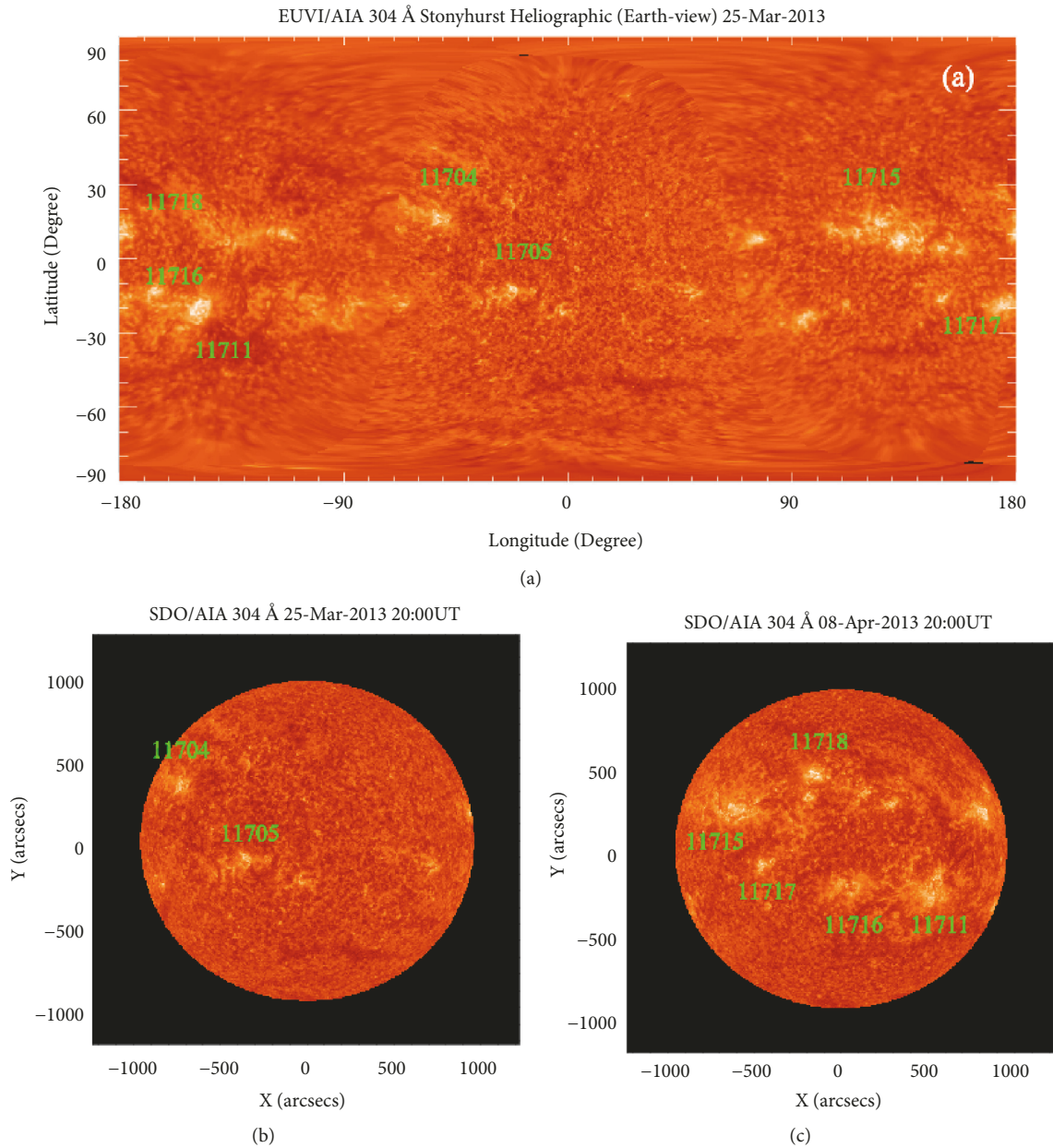


FIGURE 11: The 304 Å full-disk EUV image on 25 March 2013 (a) and Earth-side EUV images on 25 March 2013 (b) and 8 April 2013 (c).

27-day values of $F_{10.7}$ based on the solar full-disk EUV images. Moreover, to gain a more satisfactory predictive precision, combining the upcoming 1-2 days predictive values of the 54th-order AR-model with the upcoming 3-27 days predictive values of our method in practice should be considered.

Although there are problems with receiving real-time data from satellites STEREO/EUVI and SDO/AIA, this paper importantly demonstrates the tangible benefits that 360 degree solar observations provide for the prediction of solar activity. The Lagrangian 5 (L5) point lies at the third corners of the equilateral triangles in the plane of orbit whose common base is the line between the centers of Sun and

Earth. So the viewing angle in L5 point can reach -150 degrees in Stonyhurst heliographic coordinates and the L5 observing platform can provide the EUV images before about 11.25 day. If the current data could be afforded by the ability of the L5 observing platform, it would enable this technique to forecast about 11.25 days $F_{10.7}$ in practice.

Data Availability

All data used in the manuscript can be downloaded from the available database of the websites. And below are these URL of websites. (1) The $F_{10.7}$ index data used to support the findings of this study can be downloaded from the

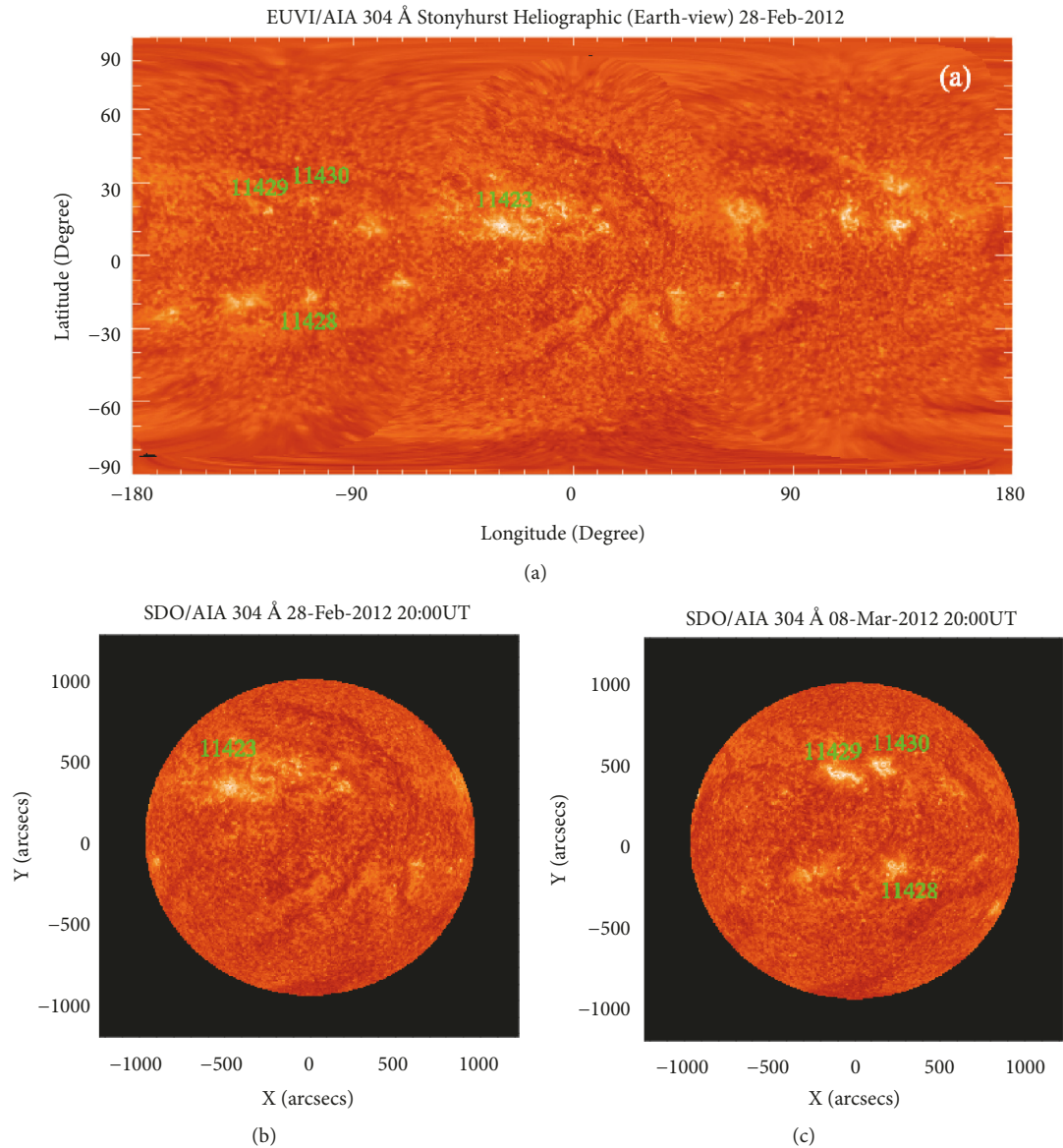


FIGURE 12: The 304 Å full-disk EUV images on 28 February 2012 (a) and Earth-side EUV images on 28 February 2012 (b) and 8 March 2012 (c).

available database of the National Oceanic and Atmospheric Administration (NOAA) (ftp://ftp.ngdc.noaa.gov/STP/space-weather/solar-data/solar-features/solar-radio/noontime-flux/penticton/penticton_observed/listings/listing_drao_noontime-flux-observed_daily.txt). (2) The daily level-1 FITS (Flexible Image Transport System) files of SDO/AIA from May 2010 to December 2015 are downloaded from the available database of the Joint Science Operations Center (JSOC) at Stanford University (<http://jsoc.stanford.edu/>). (3) The daily FITS files of STEREO/EUVI from January 2011 to December 2013 are downloaded from the available database of STEREO Science Center (<https://stereoftp.nascom.nasa.gov/data/beacon/ahead/secchi/img/euvi/> and <https://stereoftp.nascom.nasa.gov/data/beacon/behind/secchi/img/euvi/>).

Conflicts of Interest

The authors declare that they have no conflicts of interest.

Acknowledgments

The 10.7cm solar radio flux data are provided as a service by the National Research Council of Canada. We thank the SDO/AIA instrument team for providing the coronal observations and Stanford University's JSOC for providing the available database. We also thank the STEREO/EUVI instrument team and NOAA of the USA for providing their data. This work was supported by the National Defense Science and Technology Innovation Special Zone, the National

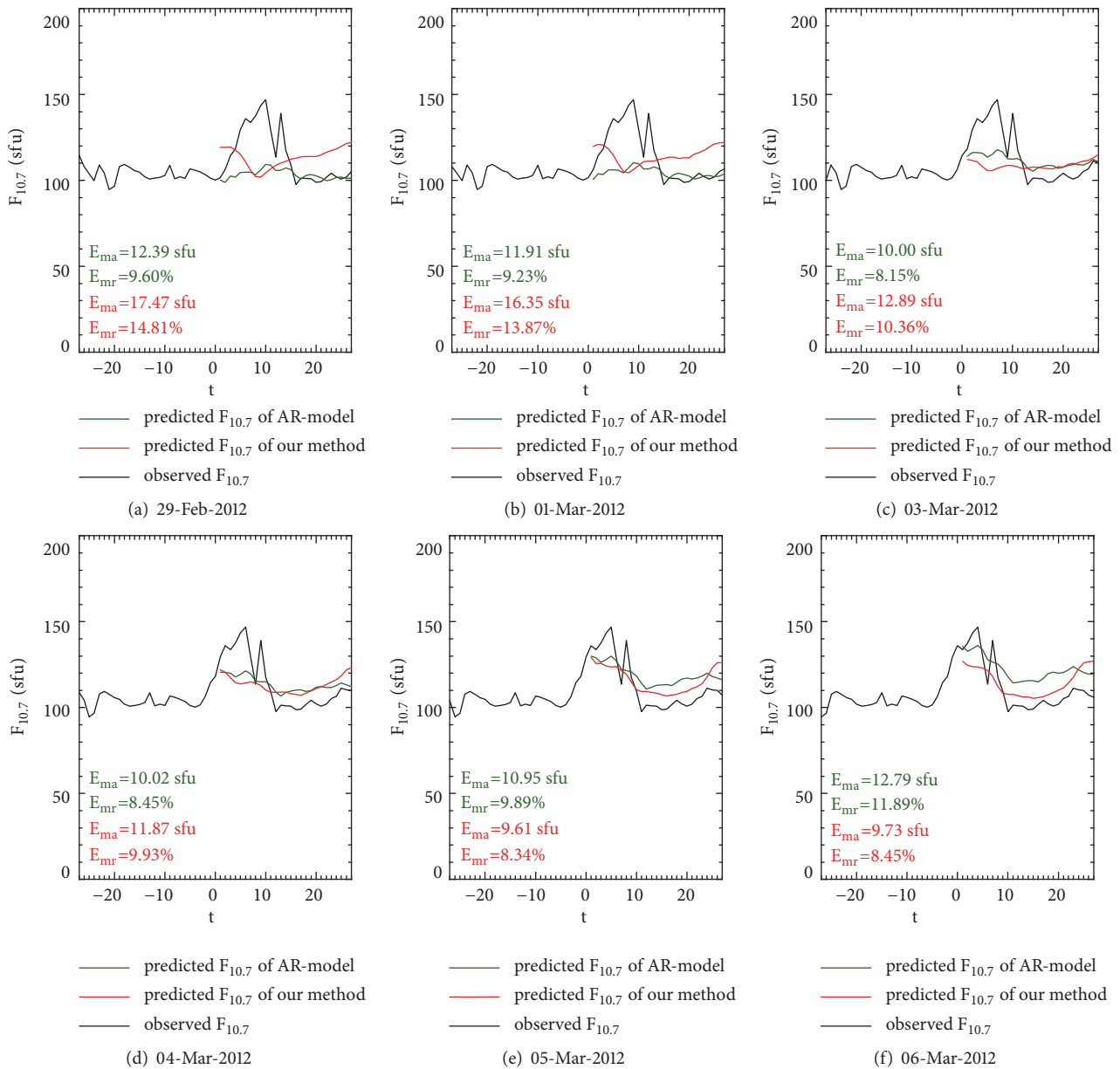


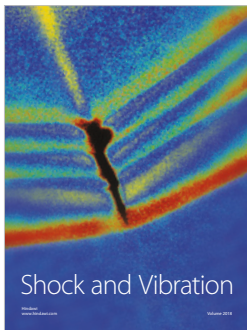
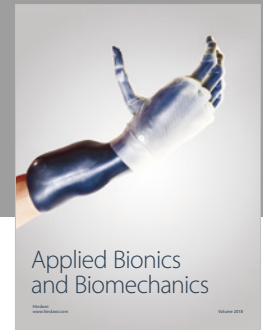
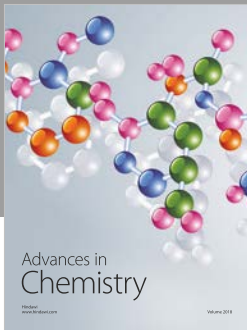
FIGURE 13: A comparison of observed $F_{10.7}$ (black line) and predictive $F_{10.7}$ obtained from AR-model (green line) and our method (red line) from 29 February 2012 to 6 March 2012.

Natural Science Foundation of China (Grant no. Y75037A070 and Grant no. 41604149), the Beijing Municipal Science and Technology Project (project number Z181100002918004), and the Strategic Priority Research Program of Chinese Academy of Sciences (Grant no. XDA17010302).

References

- [1] K. O. Kiepenheuer, "Structure and development of solar active regions," *International Astronomical Union*, vol. 35, no. 379, 1968.
- [2] H. Schunker and P. S. Cally, "Magnetic field inclination and atmospheric oscillations above solar active regions," *Monthly Notices of the Royal Astronomical Society*, vol. 372, no. 2, pp. 551–564, 2006.
- [3] R. G. Athay and J. M. Beckers, "The solar chromosphere and corona: quiet sun," *Physics Today*, vol. 29, no. 11, pp. 74–76, 1976.
- [4] J. Lee, "Radio emissions from solar active regions," *Space Science Reviews*, vol. 133, no. 1-4, pp. 73–102, 2007.
- [5] S. J. Schonfeld, S. M. White, C. J. Henney, C. N. Arge, and R. T. J. McAteer, "Coronal sources of the solar $F_{10.7}$ radio flux," *The Astrophysical Journal*, vol. 808, no. 1, 2015.
- [6] W. N. Christiansen, D. E. Yabsley, and B. Y. Mills, "Measurements of solar radiation at a wavelength of 50 centimetres during the eclipse of november 1, 1948," *Australian Journal of Chemistry*, vol. 2, no. 4, pp. 506–523, 1949.

- [7] W. Livingston, M. J. Penn, and L. Svalgaard, "Decreasing sunspot magnetic fields explain unique 10.7cm radio flux," *The Astrophysical Journal Letters*, vol. 757, no. 1, 2012.
- [8] C. L. Selhorst, J. E. Costa, C. G. Giménez de Castro et al., "The 17 GHz active region number," *The Astrophysical Journal*, vol. 790, no. 2, article 134, 2014.
- [9] K. F. Tapping, "The 10.7 cm solar radio flux ($F_{10.7}$)," *Space Weather-the International Journal of Research & Applications*, vol. 11, no. 7, pp. 394–406, 2013.
- [10] W. K. Tobiska, "Validating the solar EUV proxy, E10.7," *Journal of Geophysical Research: Space Physics*, vol. 106, no. A12, pp. 29969–29978, 2001.
- [11] A. E. Hedin, "The atmospheric model in the region 90 to 2000 km," *Advances in Space Research*, vol. 8, no. 5-6, pp. 9–25, 1988.
- [12] J. M. Picone, A. E. Hedin, D. P. Drob, and A. C. Aikin, "NRLMSISE-00 empirical model of the atmosphere: statistical comparisons and scientific issues," *Journal of Geophysical Research: Space Physics*, vol. 107, no. A12, pp. SIA15-1–SIA15-16, 2002.
- [13] S. H. Knowles, J. M. Picone, S. E. Thonnard, and A. C. Nicholas, "The effect of atmospheric drag on satellite orbits during the bastille day event," *Solar Physics*, vol. 204, no. 1-2, pp. 387–397, 2001.
- [14] D. H. Hathaway, "The solar cycle," *Living Reviews in Solar Physics*, vol. 7, no. 1, 2010.
- [15] R. Vautard, P. Yiou, and M. Ghil, "Singular-spectrum analysis: a toolkit for short, noisy chaotic signals," *Physica D: Nonlinear Phenomena*, vol. 58, no. 1–4, pp. 95–126, 1992.
- [16] H. Akaike, "Fitting autoregressive models for prediction," *Annals of the Institute of Statistical Mathematics*, vol. 21, pp. 243–247, 1969.
- [17] Z. Q. Zhong, Q. S. Liu, X. J. He, and J. C. Gong, "Application of singular spectrum analysis to solar 10.7cm radio flux 27-day forecast," *Chinese Journal of Space Science*, vol. 25, no. 3, pp. 199–203, 2005.
- [18] S. Q. Liu, Q. Z. Zhong, J. Wen, and X. K. Dou, "Modeling research of the 27-day forecast of 10.7 cm solar radio flux (I)," *Chinese Astronomy and Astrophysics*, vol. 34, no. 3, pp. 305–315, 2010.
- [19] H. B. Wang, J. N. Xiong, and C. Y. Zhao, "The mid-term forecast method of solar radiation index," *Chinese Astronomy and Astrophysics*, vol. 39, no. 2, pp. 198–211, 2015.
- [20] J. Wen, Z. Q. Zhong, and S. Q. Liu, "Model research of 10.7 cm solar radio flux 27-day forecast," *Chinese Journal of Space Science*, vol. 30, no. 3, article 198, 2010.
- [21] C. J. Henney, W. A. Toussaint, S. M. White, and C. N. Arge, "Forecasting $F_{10.7}$ with solar magnetic flux transport modeling," *Space Weather Journal*, vol. 10, article S02011, 2012.
- [22] E. Quémerais and J. L. Bertaux, "14-day forecast of solar indices using interplanetary Lyman α background data," *Geophysical Research Letters*, vol. 29, no. 2, pp. 5-1–5-4, 2002.
- [23] J. L. Bertaux, E. Kyrölä, E. Quémerais et al., *SWAN: A Study of Solar Wind Anisotropies on SOHO with Lyman Alpha Sky Mapping*, Springer, Netherlands, 1995.
- [24] C. Lindsey and D. Braun, "Seismic imaging of the sun's far hemisphere and its applications in space weather forecasting," *Space Weather-the International Journal of Research & Applications*, vol. 15, 2017.
- [25] B. O'Dwyer, G. Del Zanna, H. E. Mason, M. A. Weber, and D. Tripathi, "SDO/AIA response to coronal hole, quiet Sun, active region, and flare plasma," *Astronomy & Astrophysics*, vol. 521, article A21, 2010.
- [26] K. F. Tapping, D. Boteler, P. Charbonneau et al., "Solar magnetic activity and total irradiance since the maunder minimum," *Solar Physics*, vol. 246, no. 2, pp. 309–326, 2007.
- [27] J. R. Lemen, A. M. Title, D. J. Akin et al., "The atmospheric imaging assembly (aia) on the solar dynamics observatory (sdo)," *Solar Physics*, vol. 275, no. 1-2, pp. 17–40, 2012.
- [28] N. Balan, G. Bailey, and Y. Su, "Variations of the ionosphere and related solar fluxes during solar cycles 21 and 22," *Advances in Space Research*, vol. 18, no. 3, pp. 11–14, 1996.
- [29] K. Tapping and C. Morgan, "Changing relationships between sunspot number, total sunspot area and F10.7 in cycles 23 and 24," *Solar Physics*, vol. 292, no. 6, 2017.
- [30] R. A. Howard, J. D. Moses, D. G. Socker, K. P. Dere, and J. W. Cook, "Sun earth connection coronal and heliospheric investigation (SECCHI)," *Space Science Reviews*, vol. 136, no. 1-4, pp. 67–115, 2008.
- [31] C. Lowder, J. Qiu, R. Leamon, and Y. Liu, "Measurements of EUV coronal holes and open magnetic flux," *The Astrophysical Journal*, vol. 783, no. 142, p. 13, 2014.
- [32] J. E. Vernazza, E. H. Avrett, and R. Loeser, "Structure of the solar chromosphere. III - Models of the EUV brightness components of the quiet-sun," *The Astrophysical Journal Supplement Series*, vol. 45, no. 4, pp. 635–725, 1981.
- [33] L. D. Krista and P. T. Gallagher, "Automated coronal hole detection using local intensity thresholding techniques," *Solar Physics*, vol. 256, no. 1-2, pp. 87–100, 2009.
- [34] D. Pérez-Suárez, P. Higgins A, D. Bloomfield S et al., "Automated solar feature detection for space weather applications," *Applied Signal and Image Processing: Multidisciplinary Advancements*, pp. 207–225, 2011.
- [35] J. H. Zar, "Significance testing of the spearman rank correlation coefficient," *Journal of the American Statistical Association*, vol. 67, no. 339, pp. 578–580, 1972.
- [36] S. B. Lyerly, "The average Spearman rank correlation coefficient," *Psychometrika*, vol. 17, no. 4, pp. 421–428, 1952.
- [37] P. C. Liewer, J. Qiu, and C. Lindsey, "Comparison of helioseismic far-side active region detections with STEREO far-side euV observations of solar activity," *Solar Physics*, vol. 292, no. 10, article 146, 2017.



Hindawi

Submit your manuscripts at
www.hindawi.com

